

# Development of *Lactobacillus kimchicus* DCY51<sup>T</sup>-mediated gold nanoparticles for delivery of ginsenoside compound K: *in vitro* photothermal effects and apoptosis detection in cancer cells

Yeon-Ju Kim, Haribalan Perumalsamy, Josua Markus, Sri Renukadevi Balusamy, Chao Wang, Seong Ho Kang, Seungah Lee, Sang Yong Park, Sung Kim, Verónica Castro-Aceituno, Seung Hyun Kim & Deok Chun Yang

To cite this article: Yeon-Ju Kim, Haribalan Perumalsamy, Josua Markus, Sri Renukadevi Balusamy, Chao Wang, Seong Ho Kang, Seungah Lee, Sang Yong Park, Sung Kim, Verónica Castro-Aceituno, Seung Hyun Kim & Deok Chun Yang (2019) Development of *Lactobacillus kimchicus* DCY51<sup>T</sup>-mediated gold nanoparticles for delivery of ginsenoside compound K: *in vitro* photothermal effects and apoptosis detection in cancer cells, *Artificial Cells, Nanomedicine, and Biotechnology*, 47:1, 30-44, DOI: [10.1080/21691401.2018.1541900](https://doi.org/10.1080/21691401.2018.1541900)

To link to this article: <https://doi.org/10.1080/21691401.2018.1541900>



© 2019 The Author(s). Published by Informa UK Limited, trading as Taylor & Francis Group.



[View supplementary material](#)



Published online: 19 Jan 2019.



[Submit your article to this journal](#)



Article views: 3614



[View related articles](#)



[View Crossmark data](#)



Citing articles: 21 [View citing articles](#)

## Development of *Lactobacillus kimchicus* DCY51<sup>T</sup>-mediated gold nanoparticles for delivery of ginsenoside compound K: *in vitro* photothermal effects and apoptosis detection in cancer cells

Yeon-Ju Kim<sup>a\*</sup>, Haribalan Perumalsamy<sup>a\*</sup>, Josua Markus<sup>b</sup>, Sri Renukadevi Balusamy<sup>c</sup>, Chao Wang<sup>a</sup>, Seong Ho Kang<sup>d</sup>, Seungah Lee<sup>d</sup>, Sang Yong Park<sup>a</sup>, Sung Kim<sup>e</sup>, Verónica Castro-Aceituno<sup>a</sup>, Seung Hyun Kim<sup>a</sup> and Deok Chun Yang<sup>a,b</sup>

<sup>a</sup>Department of Oriental Medicinal Biotechnology, College of Life Science, Kyung Hee University, Yongin-si, Republic of Korea; <sup>b</sup>Graduate School of Biotechnology and Ginseng Bank, College of Life Science, Kyung Hee University, Yongin-si, Republic of Korea; <sup>c</sup>Department of Food Science and Biotechnology, Sejong University, Seoul, Republic of Korea; <sup>d</sup>Department of Applied Chemistry and Institute of Natural Sciences, College of Applied Science, Kyung Hee University, Yongin-si, Republic of Korea; <sup>e</sup>Center for Global Converging Humanities, Kyung Hee University, Yongin-si, Republic of Korea

### ABSTRACT

We report a non-covalent loading of ginsenoside compound K (CK) onto our previously reported gold nanoparticles (DCY51<sup>T</sup>-AuCKNps) through one-pot biosynthesis using a probiotic *Lactobacillus kimchicus* DCY51<sup>T</sup> isolated from Korean kimchi. The ginsenoside-loaded gold nanoparticles were characterized by various analytical and spectroscopic techniques such as field emission transmission electron microscopy (FE-TEM), energy-dispersive X-ray (EDX) spectroscopy, elemental mapping, X-ray powder diffraction (XRD), selected area electron diffraction (SAED), Fourier-transform infrared (FTIR) spectroscopy and dynamic light scattering (DLS). Furthermore, drug loading was also determined by liquid chromatography–mass spectrometry (LC–MS). In addition, DCY51<sup>T</sup>-AuNps and DCY51<sup>T</sup>-AuCKNps were resistant to aggregation caused by pH variation or a high ionic strength environment. Cell-based study confirmed that DCY51<sup>T</sup>-AuCKNps exhibited slightly higher cytotoxicity compared to ginsenoside CK treatment in A549 cells (human lung adenocarcinoma cell line) and HT29 (human colorectal adenocarcinoma cell line). Upon laser treatment, DCY51<sup>T</sup>-AuCKNps showed enhanced cell apoptosis in A549, HT29 and AGS cells (human stomach gastric adenocarcinoma cell line) compared with only DCY51<sup>T</sup>-AuCKNps treated cells. In conclusion, this preliminary study identified that DCY51<sup>T</sup>-AuCKNps act as a potent photothermal therapy agents with synergistic chemotherapeutic effects for the treatment of cancer.

### ARTICLE HISTORY

Received 15 June 2018  
Revised 10 October 2018  
Accepted 13 October 2018

### KEYWORDS

Ginsenoside CK; gold nanoparticles; photothermal therapy; photoluminescence; drug delivery; green synthesis; anticancer activity

### Introduction

The pharmacological effects of *Panax ginseng* Meyer (Korean ginseng), which has been regarded as one of the most acclaimed traditional Chinese herbal medicines for over 2000 years, can be largely accredited to its bioactive triterpenoid saponins [1]. These triterpenoid saponins, also known as ginsenosides, are further classified into three types: panaxadiol (PPD), panaxatriol (PPT) and oleanic acid [1]. The minor PPD-type ginsenosides, such as compound K (CK), often exhibit superior pharmacological effects, such as antitumour, antiaging, anticancer and anti-inflammatory activities, compared to the major glycosylated ginsenosides [1–5]. Certain limitations of ginsenoside CK exist that significantly restrict its medical applications, including the hydrophobicity of the aglycones, poor bioavailability and adverse cytotoxicity to normal cells [3]. The bioconjugation of ginsenosides to a specifically

designed drug delivery system thus plays a significant role in remediating these limitations.

Spherical gold nanoparticles are widely reported to display biocompatibility for biological applications, especially as drug carriers. In addition to their attractive optical properties as multimodality imaging agents, colloidal gold can also provide photothermal therapy (PPT) in conjunction with laser [6, 7]. Unlike conventional physical and chemical methods that often employ hazardous reducing and stabilizing agents, green synthesis of metal nanoparticles can be exploited to eliminate toxic ligands and augment nanoparticles with bioactive natural macromolecules that may render nanoparticles biologically active for biomedical applications [8]. In view of the properties, we used DPPH-scavenging gold nanoparticles (DCY51<sup>T</sup>-AuNps) synthesized by bacteria as nanocarriers to deliver ginsenoside CK and improve its water dispersibility and anticancer effects.

**CONTACT** Yeon-Ju Kim ✉ [yeonjukim@khu.ac.kr](mailto:yeonjukim@khu.ac.kr); Deok Chun Yang ✉ [dcyang@khu.ac.kr](mailto:dcyang@khu.ac.kr) Department of Oriental Medicinal Biotechnology, College of Life Science, Kyung Hee University, Yongin-si, Gyeonggi-do 446-701, Republic of Korea

\*Both authors contributed equally to this work.

 Supplemental data for this article can be accessed at <http://10.1080/21691401.2018.1541900>

© 2019 The Author(s). Published by Informa UK Limited, trading as Taylor & Francis Group.

This is an Open Access article distributed under the terms of the Creative Commons Attribution License (<http://creativecommons.org/licenses/by/4.0/>), which permits unrestricted use, distribution, and reproduction in any medium, provided the original work is properly cited.

The use of PTT is a recently developed technique and an advanced therapeutic strategy which utilize the near infrared laser photo absorbers to trigger heat for thermal excision of cancer cells upon NIR irradiation [9–11]. When compared with conventional therapies, the use of PTT exhibits distinct advantages in cancer therapy including enhanced specificity, reduction in invasion and precise spatial-temporal selectivity and so on [12, 13]. PTT can directly obliterate the cancer cells in early stage and local metastasis and even to treat metastasis. Several previous reports make use of PTT in treating cancer cell metastasis [14–16]. The efficacy of PTT depends on the transformation of light to heat with photothermal agents especially nanoscales agents.

In our study, DCY51<sup>T</sup>-AuNps were prepared following our previously published method via an intracellular membrane-bound mechanism by lactic acid-producing *Lactobacillus kimchicus* DCY51<sup>T</sup>. The utilization of fresh biomass to synthesize gold nanoparticles is preferred than intracellular enzymes due to the recovery of nicotinamide adenine dinucleotide (NADH)-dependent coenzymes involved in the reduction of Au<sup>3+</sup> ion [17, 18]. Herein, ginsenoside CK was non-covalently bioconjugated to probiotic-mediated DCY51<sup>T</sup>-AuNps. Similarly, model drugs, such as hydrophobic doxorubicin and antibacterial rifaximin, were capable to be loaded onto DCY51<sup>T</sup>-AuNps by the same methodology. The complexation of drug by DCY51<sup>T</sup>-AuNps was further characterized by spectroscopic and analytical techniques. Drug loading was determined by liquid chromatography–mass spectrometry (LC–MS). The preliminary *in vitro* anticancer effects and PPT against lung (A549), colon (HT29) and stomach (AGS) adenocarcinoma cells of the biosynthesized ginsenoside CK-loaded gold nanoparticles (DCY51<sup>T</sup>-AuCKNps) were subsequently investigated. Finally, DCY51<sup>T</sup>-AuCKNps could be easily detected and developed to be a cancer cell diagnostic tool using real-time monitoring technologies.

## Experimental

### Materials

MRS (de Man, Rogosa and Sharpe) broth and agar were purchased from MBcell (Seoul, Republic of Korea). Analytical grade hydrogen tetrachloroaurate (III) hydrate (gold salt) and hydrochloric acid (HCl, ACS reagent, 37%) were purchased from Sigma-Aldrich Chemicals (St. Louis, MO). Sodium chloride (NaCl, ≥99.50%) and sodium hydroxide (NaOH, ≥98%) were purchased from Daejung Chemicals and Metals Co., Ltd. (Shiheung-city, Korea). Ginsenoside CK (≥K%) was acquired from Ginseng Bank, Kyung Hee University (Yongin, Republic of Korea). Doxorubicin-hydrochloride and rifaximin were purchased from Cayman Chemical Company (Ann Arbor, MI). Premade phosphate-buffered saline (20× PBS) was purchased from Biosesang (Seongnam, Republic of Korea). Methyl alcohol (MeOH, 95%) was procured from Samchun Pure Chemical Co. Ltd. (Pyeongtaek, Republic of Korea). Other chemicals were obtained from commercial suppliers and used as received.

### Cell lines

RAW264.7 (murine leukemic macrophage cell line) and A549 cells (human lung adenocarcinoma cell line) were obtained

from Korean Cell Line Bank (KCLB, Seoul, Republic of Korea). HT29 (human colorectal adenocarcinoma cell line) and AGS cells (human stomach adenocarcinoma cell line) were obtained from American Type Culture Collection (ATCC, Manassas, VA). Dulbecco's modified Eagle medium (DMEM), foetal bovine serum (FBS), RPMI 1640 culture media and penicillin–streptomycin solution were purchased from GenDEPOT (Barker, TX). Soluble 3-(4,5-dimethylthiazol-2-yl)-2,5-diphenyl-tetrazolium bromide (MTT) was purchased from Life Technologies (Eugene, OR). Other chemicals were obtained from commercial suppliers and used as received.

### Bacterial culture condition for the biological synthesis of DCY51<sup>T</sup>-AuCKNps

The bacterial strain was isolated from traditional Korean kimchi as type strain *Lactobacillus kimchicus* DCY51<sup>T</sup> (KCTC 12976<sup>T</sup>, JCM 15530<sup>T</sup>) by Liang et al. [19]. The GenBank/EMBL/DBJ accession numbers for the 16S rRNA gene and pheS sequences of strain DCY51<sup>T</sup> are EU678893 and FJ904276, respectively [19]. The isolated strain was streaked on MRS agar and then incubated at 37 °C for 48 h. Bacterial cells were inoculated into 100 mL MRS broth and incubated at 37 °C and 100×g for 24 h. After incubation, 10 mL of the inoculated culture broth was further centrifuged at 6300×g for 5 min. Fresh biomass was collected and used for the one-pot biological synthesis of gold nanoparticles according to our previous study [20].

### Synthesis of DCY51<sup>T</sup>-AuCKNps

DCY51<sup>T</sup>-AuNps were synthesized by *L. kimchicus* DCY51<sup>T</sup> according to a previous method by Markus et al. with minor modifications [20]. The collected biomass was washed with 10 mM PBS buffer and re-suspended in 25 mL of sterilized dH<sub>2</sub>O. 1 mM gold salt and 1 mg ginsenoside CK (1.6 mM, Mw 622.884) were added and incubated at 37 °C and shaken at 150×g in the dark. Following the addition of the gold salt solution into the microbial cell suspension in dH<sub>2</sub>O, the synthesis of DCY51<sup>T</sup>-AuCKNps was detected visually by a change in the colour of the biomass in the reaction mixtures. Thereafter, the dark purple-coloured reaction mixtures were centrifuged at 2500×g for 5 min to remove supernatant and unloaded drugs. To collect the trapped, drug-loaded nanoparticles from the bacterial cells, the bacterial pellets underwent alternating cycles of ultra-sonication and continuous centrifugation at 2500×g for 5 min. Drug-loaded DCY51<sup>T</sup>-AuCKNps were collected by high speed centrifugation at 28,000×g for 10 min and were washed exhaustively with dH<sub>2</sub>O. Finally, DCY51<sup>T</sup>-AuNps and DCY51<sup>T</sup>-AuCKNps were stored as aqueous suspensions at 4 °C until needed for experiments. Solid specimens were obtained by air-drying nanoparticles overnight. In addition, commercially available drugs such as, doxorubicin and rifaximin were also loaded to DCY51<sup>T</sup>-AuNps to synthesize DCY51<sup>T</sup>-DoxorubicinNps and DCY51<sup>T</sup>-RifaximinNps, respectively, using the same aforementioned protocol.

### High resolution transmission electron microscopy (HR-TEM) ultra-microtome analysis of DCY51<sup>T</sup>-AuCKNps

Prior to HR-TEM analysis, 2.5% of glutaraldehyde in 1 M PBS buffer was added to nanoparticle suspension. The sample was washed thrice with  $1 \times 0.1$  M PBS buffer for 5 min. The supernatant was removed and 1% OsO<sub>4</sub> was added and allowed to react for 1 h. The sample was washed thrice with  $1 \times 0.1$  M PBS buffer for 10 min. Next, the sample was washed twice using dH<sub>2</sub>O for 5 min. Then, ethanol was added for dehydration and further steps were followed by the standard protocol [22]. Subsequently, ultra-thin-sectioned samples were prepared for HR-TEM. The sectioned samples were stained with uranyl acetate for 10 min and lead citrate for 1 min prior to analysis. The isolated strains *L. kimchicus* DCY51<sup>T</sup> and *L. brevis* DCY65 were used as biofactories for gold nanoparticles loaded with ginsenoside CK.

### Characterization of nanoparticles

The concentration of gold nanoparticles was estimated by the equation derived by Haiss et al. whereas the particle diameter was estimated by the Debye–Scherrer formula with a shape factor (*K*) of 0.9 [22, 23]. The absorbance spectra of the drug-loaded nanoparticle suspension were scanned in the range of 300–800 nm with an ultraviolet–visible (UV–vis) spectrophotometer (Ultrospec™ 2100 pro) with a quartz cuvette having a 10 mm path length (2100 Pro, Amersham Biosciences Corp., Piscataway, NJ). Field emission transmission electron microscopy (FE-TEM) and HR-TEM were assessed with a JEM-2100F operated at 200 kV (JEOL, Peabody, MA). FE-TEM images were obtained by spreading droplets of aqueous suspension of drug-loaded DCY51<sup>T</sup>-AuCKNps onto a carbon-coated copper grid and drying at 60 °C. X-ray powder diffraction (XRD) spectra were obtained with a D8 Discover diffractometer with a general area detector diffraction system (Bruker, Hamburg, Germany) operating at a voltage of 40 kV and 40 mA with CuK $\alpha$  radiation of 1.54 Å in the  $2\theta$  range of 20–80°. The zeta potential and hydrodynamic particle size of the drug-loaded DCY51<sup>T</sup>-AuCKNps suspended in dH<sub>2</sub>O were determined with an ELS-Z2 series zeta potential and particle size analyser (Otsuka Electronics Co. Ltd., Osaka, Japan) at 25 °C. Pure water with a refractive index of 1.3328, viscosity of 0.8878 and dielectric constant of 78.3 was used as refer-

ence. Fourier-transform infrared (FTIR) spectra of ginsenoside CK and the corresponding drug-loaded DCY51<sup>T</sup>-AuCKNps were recorded on a PerkinElmer Spectrum 100 spectrometer (PerkinElmer, Waltham, MA). The air-dried nanoparticle powder was scanned in the range of 4000–450 cm<sup>-1</sup> at a resolution of 4 cm<sup>-1</sup> on KBr pellets. Furthermore, the *in vitro* stability of DCY51<sup>T</sup>-AuNps and DCY51<sup>T</sup>-AuCKNps over a wide range of pH and electrolyte conditions was assessed. The stability of nanoparticles under different pH and ionic strength conditions is an important criterion for their biomedical application [25]. The intracellular pH of tumour tissues (pH 5.0–6.5) is often more acidic than the physiological pH conditions of normal tissues (pH 7.4) [26]. The stability of DCY51<sup>T</sup>-AuCKNps in an aqueous suspension was demonstrated over a wide range of pH conditions (pH 2–10) by adjustment with 0.1 M HCl and 0.2 M NaOH at room temperature. In addition, DCY51<sup>T</sup>-AuCKNps was also suspended in different electrolyte conditions (10<sup>-1</sup> to 10<sup>-5</sup> M) by addition of NaCl. The lack of changes in the surface plasmon resonance (SPR) peak and band, as measured by UV–vis spectrophotometer after incubation, indicates the colloidal stability of nanoparticles in all of the above conditions [8].

### Photoluminescence spectra of DCY51<sup>T</sup>-AuCKNps

The photoluminescence (PL) spectra were measured at room temperature using a fixed 325 nm line of a HeCd laser as the excitation source. Emitted light was collected by a lens and analysed using a grating monochromator and a GaAs photomultiplier tube. Standard lock-in detection techniques were used to maximize the signal-to-noise ratio. The laser power for the PL excitation was 5.66 W/cm<sup>2</sup>.

### Drug loading efficiency

The drug loading of DCY51<sup>T</sup>-AuCKNps was determined by LC–MS. The amount of CK loaded onto the nanoparticles was quantified by LC–MS. Briefly, 3 mg of air-dried drug-loaded DCY51<sup>T</sup>-AuNps was suspended in dimethyl sulphoxide (DMSO)–MeOH mixture (1:4, v/v). The nanoparticle suspension was sonicated overnight to ensure complete release of drug into MeOH mixture. The supernatant was collected by filtration and the amount of released drug was quantified using an LC–MS instrument (Agilent Technologies 6410 Triple Quad, Kromasil C18 column (2.1 mm  $\times$  100 mm, 2.7  $\mu$ m), Santa Clara, CA) with distilled water (solvent A) and MeOH (solvent B) as mobile phases at 5% B and 95% A for 0 min, 60% B and 40% for 15 min, 100% B for 18 min, 100% B for 30 min, 5% B and 95% A for 32 min and 5% B and 95% A for 32 min, all at a flow rate of 0.4 mL/min. The injection volume of each sample was 1  $\mu$ L. UV detection was performed at 203 nm. Drug loading efficiency was calculated by the following formula:

$$\text{Drug loading efficiency (\%)} = \frac{\text{Total amount of drug released from nanoparticles}}{\text{Yield of nanoparticles}} \times 100\%$$

ence. Fourier-transform infrared (FTIR) spectra of ginsenoside CK and the corresponding drug-loaded DCY51<sup>T</sup>-AuCKNps were recorded on a PerkinElmer Spectrum 100 spectrometer (PerkinElmer, Waltham, MA). The air-dried nanoparticle powder was scanned in the range of 4000–450 cm<sup>-1</sup> at a resolution of 4 cm<sup>-1</sup> on KBr pellets. Furthermore, the *in vitro* stability of DCY51<sup>T</sup>-AuNps and DCY51<sup>T</sup>-AuCKNps over a wide range of pH and electrolyte conditions was assessed. The

### Estimation of gold ion content in DCY51<sup>T</sup>-AuCKNps by ICP/QMS

The gold content of DCY51<sup>T</sup>-AuCKNps was measured by an inductively coupled plasma/quadrupole-mass spectrometer (ICP/QMS) using a previously published method [27]. Analysis was carried out using a NexION 300D (PerkinElmer, Waltham, MA). Briefly, 0.5 g of DCY51<sup>T</sup>-AuCKNps were hydrolysed with

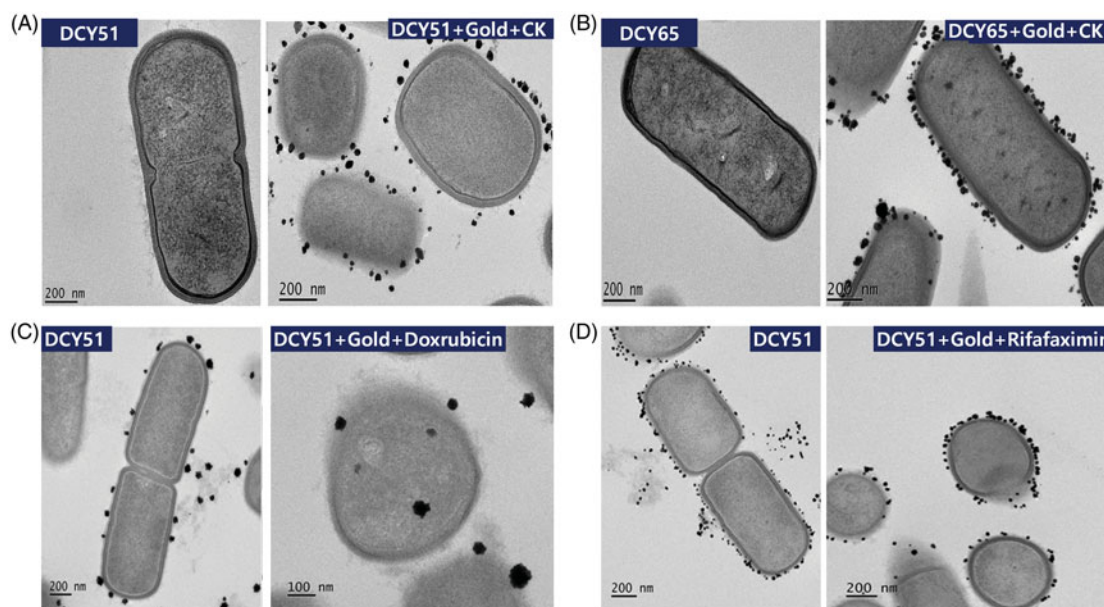


**Figure 1.** HR-TEM analysis of (A) DCY51<sup>T</sup>-AuCKNps and (B) DCY65<sup>T</sup>-AuCKNps which were derived from two different *Lactobacillus* strains: *L. kimchicus* DCY51<sup>T</sup> and *L. brevis* DCY65, respectively. HR-TEM analysis of model drug compounds derived from *Lactobacillus kimchicus* DCY51<sup>T</sup>. (C) DCY51<sup>T</sup>-DoxorubicinNps. (D) DCY51<sup>T</sup>-RifaximinNps.

HCl and heated at 180 °C for drying. Then, a mixture of HCl and HNO<sub>3</sub> solution was added to the suspension to reach a final volume of 10 mL. A radio frequency (RF) power of 1600 W, a coolant gas flow rate of 18 L/min, an auxiliary gas flow rate of 1.30 L/min and a nebulizer gas flow rate of 1.02 mL/min were used for the analysis.

### In vitro cell cytotoxicity of DCY51<sup>T</sup>-AuCKNps

Cytotoxicity analysis was conducted via MTT assay in RAW264.7, HaCaT, A549 and HT29 cells according to our previous studies [28, 29]. To investigate the cytotoxicity of drug-loaded DCY51<sup>T</sup>-AuNps and free ginsenoside CK, the cells were treated with various concentrations of drug-loaded DCY51<sup>T</sup>-AuCKNps and free drug at 37 °C for 48 h at 90% confluency. Finally, the absorbance of each coloured solution was quantified by an enzyme-linked immunosorbent assay reader (Bio-Tek Instruments, Inc., Winooski, VT) at 570 nm. The optical density of formazan formed in untreated cells (negative control) represented 100% cell viability.

Furthermore, the antiproliferative activity of DCY51<sup>T</sup>-AuCKNps towards the human stomach cancer cell lines (AGS) was evaluated using an MTT assay after treatment with an IR beam. After adhesion, DCY51<sup>T</sup>-AuCKNps at different concentrations were added to 96 well plates. Based on the preliminary test results, the anti-proliferative activity of DCY51<sup>T</sup>-AuCKNps was determined with three different concentrations ranging from 25 to 100 μL in 0.1% DMSO. Before treatment, all wells except the control well were illuminated with a laser beam for approximately 3 min at 800 nm. The culture plates were incubated for 48 h in a 37 °C, humidified atmosphere containing 5% CO<sub>2</sub>. The plates were then washed with 100 μL PBS and 100 μL of 0.05% MTT reagent was added to each well and then incubated for 4 h at the same conditions as stated previously. The MTT solution was removed and

200 μL DMSO was added to each well. Finally, the plate was shaken in a microplate shaker for 10 min to dissolve the purple formazan crystals. 5-Fluorouracil served as a positive control and was similarly formulated. The DMSO solution was used as a negative control.

### In vitro photothermal therapy and Hoechst nuclear staining assay

RAW264.7, AGS, A549 and HT29 cells were seeded onto glass coverslips and incubated in six-well plates at a density of  $2.5 \times 10^5$  cells/mL for 24 h at 37 °C in a humidified incubator with 5% CO<sub>2</sub> and 95% air. The cells were then incubated with a suspension of DCY51<sup>T</sup>-AuNps or DCY51<sup>T</sup>-AuCKNps (1 or 5 μg/mL; equivalent to 0.18 and 0.89 μM of ginsenoside CK) for 24 h. Next, the cells were washed with 1 × PBS to remove excess nanoparticles and fixed with 3.7% (v/v) formaldehyde for 5 min at room temperature. The cells were further incubated in fresh culture medium for 24 h. Subsequently, RAW264.7, A649 and HT29 cells were irradiated with a 635 nm laser (Shanghai Dream Laser Technology Co. Ltd., Shanghai, China) with a heat flux density of 0.74 W/cm<sup>2</sup> directly above the cell plates for 10 min with a laser spot size of 0.2 cm<sup>2</sup>, resulting in a total energy dose of 88.80 J. On the other hand, AGS cells were irradiated with an 800 nm laser. After irradiation, the cells were maintained at 37 °C in a humidified incubator with 5% CO<sub>2</sub>. Finally, the irradiated cells were stained by Hoechst 33258 solution (2 μg/mL) for 20 min in the dark at room temperature to analyse synergistic cell apoptosis [30]. Images of Hoechst stain were acquired by a fluorescence microscope (×400, Optinity, Korean Labtech, Namyangju, South Korea). In all studies, cells without nanoparticles and cells incubated with DCY51<sup>T</sup>-AuNps at 5 μg/mL served as blank and negative control and were subjected to

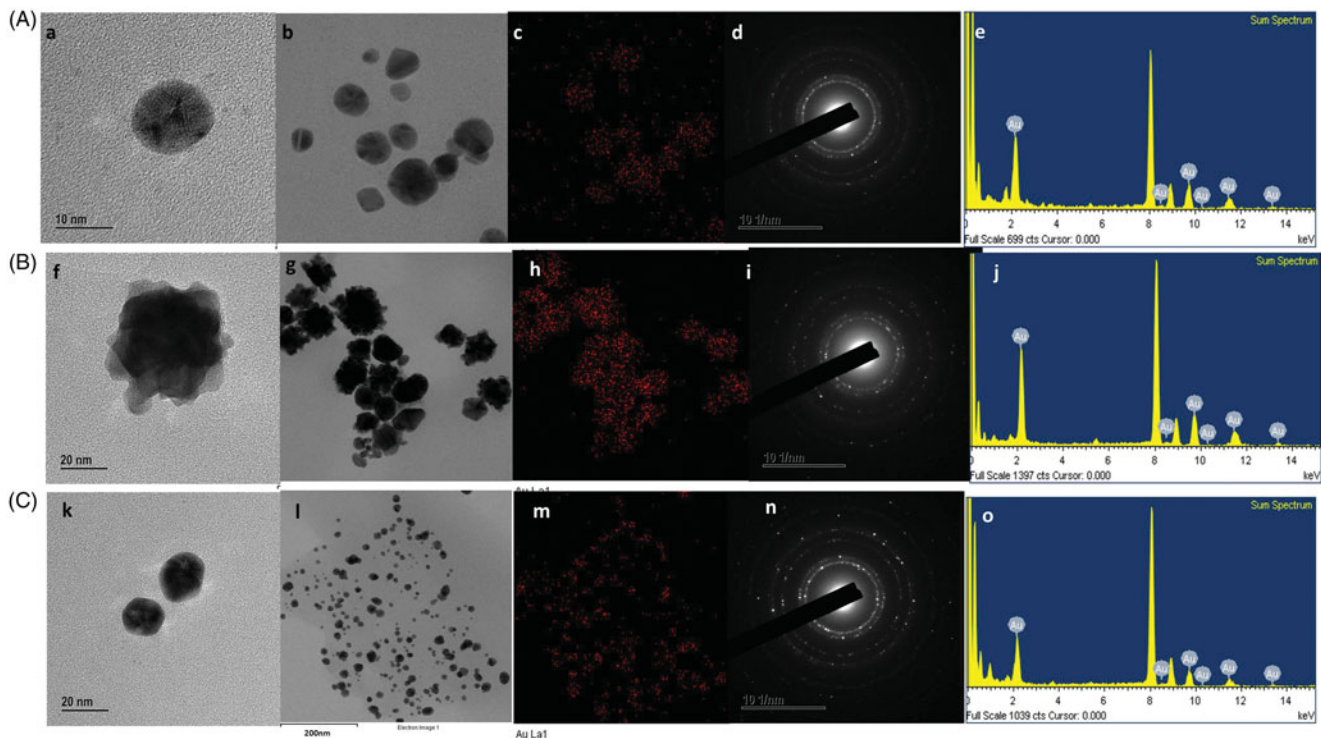


**Figure 2.** TEM analysis of (A) DCY51<sup>T</sup>-AuCKNps, (B) DCY51<sup>T</sup>-DoxorubicinNps and (C) DCY51<sup>T</sup>-RifaximinNps. TEM images of (a, b) DCY51<sup>T</sup>-AuCKNps, (f, g) DCY51<sup>T</sup>-DoxorubicinNps and (k, l) DCY51<sup>T</sup>-RifaximinNps. Gold distribution of (c) DCY51<sup>T</sup>-AuCKNps, (h) DCY51<sup>T</sup>-DoxorubicinNps and (m) DCY51<sup>T</sup>-RifaximinNps. SAED of (d) DCY51<sup>T</sup>-AuCKNps, (i) DCY51<sup>T</sup>-DoxorubicinNps and (n) DCY51<sup>T</sup>-RifaximinNps. EDX of (e) DCY51<sup>T</sup>-AuCKNps, (j) DCY51<sup>T</sup>-DoxorubicinNps and (o) DCY51<sup>T</sup>-RifaximinNps.

the same irradiation conditions as cells incubated with DCY51<sup>T</sup>-AuCKNps.

### Total internal reflection scattering (TIRS)/differential interference contrast (DIC) detection system

TIRS microscopy was carried out on an upright Olympus BX51 microscope (Olympus Optical Co., Ltd., Tokyo, Japan) equipped with a 100 $\times$  oil iris objective lens (NA=0.6–1.3, UPLANFLN, Olympus Optical Co., Ltd., Tokyo, Japan). TIRS illumination was used, with a 30 mW, 637 nm laser (MGL-III-637–200 mW, Changchun New Industries Optoelectronics Tech. Co., Ltd., Changchun, China) for illumination of the gold nanoparticles. A Uniblitz mechanical shutter (model LS3S2ZO-R3, Vincent Associates, Rochester, NY) and a driver (model VMM-D1, Vincent Associates, Rochester, NY) were synchronized to the electron-multiplying cooled charge-coupled device camera (512 $\times$ 512 pixel imaging array, QuantEM 512SC, Tucson, AZ). The exposure time was 100 ms and wavelength selection was accomplished with a central wavelength of 620/14 nm purchased from Semrock (Rochester, NY). A lab-made DIC system was modified from previously published configurations [31]. The illumination light was provided by a 100 W halogen lamp. All images were obtained with the MetaMorph 7.5 software (Universal Imaging, Sunnyvale, CA).

### Statistical analysis

All experiments were performed at least in triplicates unless stated otherwise. Values shown are reported as means $\pm$ SDs.

The statistical significances between control and sample groups were evaluated by Student's *t*-test. A greater extent of statistical significances was assigned with increasing number of asterisks (\* $p$ <.05, \*\* $p$ <.01, \*\*\* $p$ <.001 and \*\*\*\* $p$ <.0001).

## Results and discussion

### One-pot biosynthesis of DCY51<sup>T</sup>-AuCKNps

Following the addition of 1 mM of gold salt and 1 mg ginsenoside CK into the biomass suspension, the colour of the cell biomass changed to pinkish purple at 4 h and then consequently became deep purple after 12 h. No further colour change was observed after 12 h of incubation. This observation was consistent with our previous study [20]. The growth medium alone and cell biomass without gold salt (negative control) did not exhibit any colour changes. The colloidal nanoparticles excite the free electrons and may result in oscillations, which reverberate with the frequency of visible light wavelengths. This SPR phenomenon is responsible for the absorption in the visible spectrum and thus the distinct purple colour of the synthesized DCY51<sup>T</sup>-AuNps and DCY51<sup>T</sup>-AuCKNps [32].

Upon further investigation by HR-TEM (Figure 1(A)), the formation of DCY51<sup>T</sup>-AuCKNps was more concentrated upon the bacterial capsule and cell wall than on the cytoplasmic membrane, possibly due to the reduction of the metal ions by the enzymes and exopolysaccharides (EPSs) present in the cell wall and slime layer. Few of the nanoparticles were found to be transported into the cytoplasmic membrane where they further aggregated. If the reaction could proceed for a longer time, more diversity in the size of

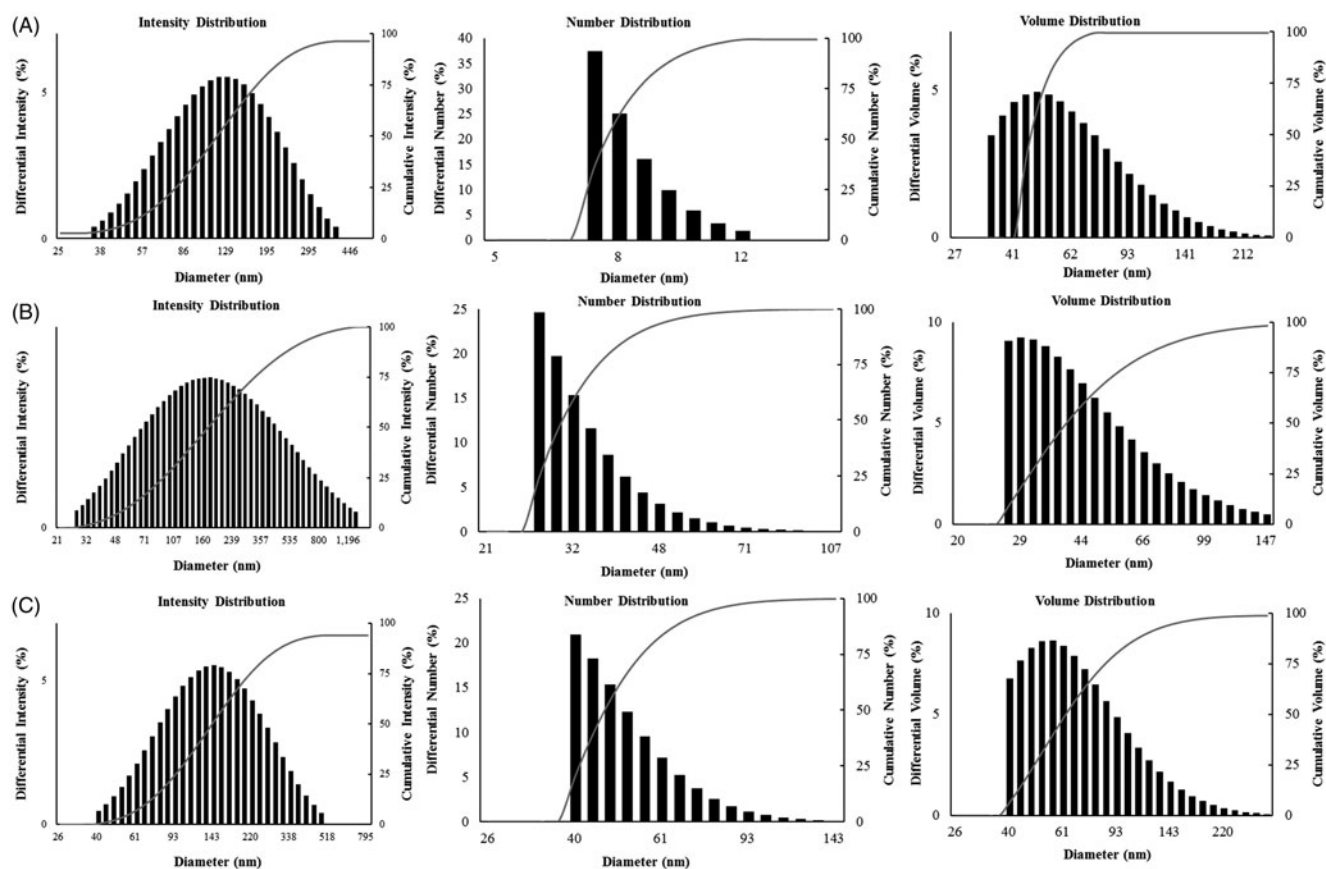


**Figure 3.** Particle size distribution (DLS) of the obtained nanoparticles with respect to intensity, number and volume. (A) DCY51<sup>T</sup>-AuCKNps. (B) DCY51<sup>T</sup>-DoxorubicinNps. (C) DCY51<sup>T</sup>-RifaximinNps.

DCY51<sup>T</sup>-AuCKNps was found [17, 31, 32]. Our sample was collected after 12 h of incubation. As anticipated, negative control did not exhibit the formation of gold nanoparticles. For comparison, *L. brevis* DCY65 was also used as biofactories for gold nanoparticles synthesis (Figure 1(B)). Similarly, to *L. kimchicus* DCY51<sup>T</sup>, the formation of DCY65-AuCKNps was localized on the surface of bacterial cells with some aggregated in the cell wall.

Up to now the exact mechanism of green synthesis has not yet been fully elucidated, even though some reports have presented the intracellular synthesis of AuNps by *Lactobacillus* species [17, 19, 31]. It has been postulated that EPSs and NADH-dependent oxido-reductase secreted by the microorganism on the bacterial membranes were responsible for the reduction of gold ions, and membranous phospholipid, organic acids and amino acid residues inside the cells were responsible for providing stabilization of the nanoparticle's carboxylate groups via electrostatic interaction. The metal nuclei and bacterial membranous substances interacted to form nanoparticles through further reduction and aggregation [18, 32]. Several non-covalent interactions, including electrostatic interactions, hydrogen bonds, hydrophobic forces and van der Waals forces, were conjectured to play key roles in the binding process of proteins with ginsenoside CK to the surface of DCY51<sup>T</sup>-AuNps [25]. Furthermore, poorly water soluble ginsenoside CK might also move into the hydrophobic micro-regions of the proteins stabilizing the nanoparticles [34]. In addition to DCY51<sup>T</sup>-AuCKNps, DCY51<sup>T</sup>-

DoxorubicinNps (Figure 1(C)) and DCY51<sup>T</sup>-RifaximinNps (Figure 1(D)) were also synthesized by *L. kimchicus* DCY51<sup>T</sup>. Similarly, gold nanoparticles were found inside the cell envelope or on the surface. Some were formed in the loose slime layers that had trailed off into the medium. This observation suggested that metal ion reduction and stabilization might be localized within cell envelope or cell surface by enzymes or EPS present in the cell wall and slime layer.

### FE-TEM analysis of DCY51<sup>T</sup>-AuCKNps, DCY51<sup>T</sup>-DoxorubicinNps and DCY51<sup>T</sup>-RifaximinNps

DCY51<sup>T</sup>-AuCKNps (Figure 2(A)), DCY51<sup>T</sup>-DoxorubicinNps (Figure 2(B)) and DCY51<sup>T</sup>-RifaximinNps (Figure 2(C)) were further analysed by FE-TEM. The FE-TEM images showed spherical DCY51<sup>T</sup>-AuCKNps, DCY51<sup>T</sup>-DoxorubicinNps and DCY51<sup>T</sup>-RifaximinNps with varying sizes of 10–40 nm, 20–60 nm and 10–20 nm, respectively. Figure 2(a,f,k) reveals that the DCY51<sup>T</sup>-AuCKNps and DCY51<sup>T</sup>-RifaximinNps were spherical while the DCY51<sup>T</sup>-DoxorubicinNps aggregated further to form flower-shaped nanostructures. The distributions of gold were clearly visible in the electron image of DCY51<sup>T</sup>-AuCKNps (Figure 2(c)), DCY51<sup>T</sup>-DoxorubicinNps (Figure 2(h)) and DCY51<sup>T</sup>-RifaximinNps (Figure 2(m)), respectively. Energy-dispersive X-ray (EDX) spectroscopy of DCY51<sup>T</sup>-AuCKNps (Figure 2(e)), DCY51<sup>T</sup>-DoxorubicinNps (Figure 2(j)) and DCY51<sup>T</sup>-RifaximinNps (Figure 2(o)) determined the highest

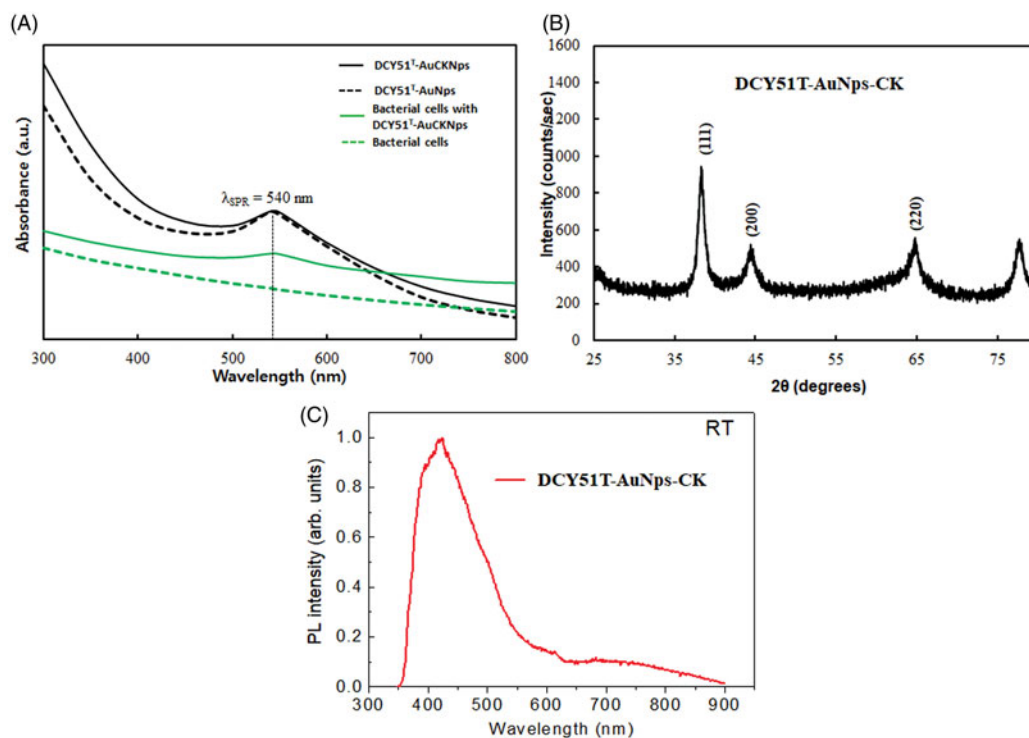


**Figure 4.** (A) UV-vis spectra of DCY51<sup>T</sup>-AuNps, with and without ginsenoside CK. (B) XRD spectrum of DCY51<sup>T</sup>-AuCKNps. (C) Photoluminescence of DCY51<sup>T</sup>-AuCKNps.

optical absorbance band peaks to be at 2.3 keV, which corresponded to the characteristic peak of metallic gold [35].

#### **Particle size distribution of DCY51<sup>T</sup>-AuCKNps, DCY51<sup>T</sup>-DoxorubicinNps and DCY51<sup>T</sup>-RifaximinNps**

The size distribution profile of DCY51<sup>T</sup>-AuCKNps (Figure 3(A)), DCY51<sup>T</sup>-DoxorubicinNps (Figure 3(B)) and DCY51<sup>T</sup>-RifaximinNps (Figure 3(C)) was determined using a particle size analyser with respect to intensity, number and volume. Similar to our previously reported DCY51<sup>T</sup>-AuNps, DCY51<sup>T</sup>-AuCKNps, DCY51<sup>T</sup>-AuDoxorubicinNps and DCY51<sup>T</sup>-AuDoxorubicinNps synthesized by strain DCY51<sup>T</sup> were not entirely monodisperse as observed from the FE-TEM results in Figure 2 [20]. This polydispersity was also apparent from the wide size distribution of the intensity-based histogram (Figure 3(A–C)). The average hydrodynamic diameter of DCY51<sup>T</sup>-AuCKNps was determined to be  $134.25 \pm 1.63$  nm with a PDI of  $0.13 \pm 0.001$ . Contrary to our previously published dynamic light scattering (DLS) result of DCY51<sup>T</sup>-AuNps [20], the Z-average value of the drug-loaded nanoparticles demonstrated a modest growth. This behaviour was also observed in DCY51<sup>T</sup>-AuDoxorubicinNps (Figure 3(B)) and DCY51<sup>T</sup>-AuRifaximinNps (Figure 3(C)). This result indicated the loading of ginsenoside CK, doxorubicin and rifaximin on the surface of DCY51<sup>T</sup>-AuNps [36]. At neutral pH in dH<sub>2</sub>O, the zeta potential ( $\zeta$ ) of DCY51<sup>T</sup>-AuNps and DCY51<sup>T</sup>-AuCKNps was recorded to be  $\sim 51.04$  mV and  $\sim 52.22$  mV, respectively, implying that the nanoformulations were stable in the aqueous suspension. The small increase in the positive charge indicated that other attractive forces, such as van der Waals forces or hydrogen bonding, might be responsible for

facilitating the drug loading process [27]. According to previous studies, nanoparticles of  $\leq 200$  nm may accumulate in tumour tissues due to the enlarged gap junctions (0.1–2  $\mu$ m) in the poorly aligned and defective endothelia lining. This enhanced permeability and retention (EPR) effect is the main mechanism of non-targeted drug delivery system [37]. Furthermore, the cationic charge of DCY51<sup>T</sup>-AuCKNps may induce higher cellular uptake and greater cytotoxicity to cancer cells due to the permeability of the anionic cell membrane [38].

#### **UV-vis spectra analysis, XRD profile and photoluminescence spectroscopy of DCY51<sup>T</sup>-AuCKNps**

UV-vis spectroscopy was used to monitor the visible absorption bands of the nanoparticles. These absorption bands are strongly dependent on the nanoparticle size, shape, surface and agglomeration state [22, 39, 40]. Nanoparticles with larger crystallite sizes or particle agglomeration often have broad absorption bands spanning into the red-shifted range ( $>600$  nm) due to the presence of both transversal and longitudinal SPRs [41]. Likewise, the extinction spectra of DCY51<sup>T</sup>-AuCKNps exhibited a major absorbance peak at  $\sim 540$  nm after 12 h of incubation at 37 °C (Figure 4(A)). There was no change in the SPR peak between drug-loaded nanoparticles (DCY51<sup>T</sup>-AuCKNps) and DCY51<sup>T</sup>-AuNps, meaning that there was no significant change in the size, shape, surface and agglomeration state of the two nanoparticles. The sharpness of the SPR peaks of DCY51<sup>T</sup>-AuNps and DCY51<sup>T</sup>-AuCKNps revealed that the biosynthesized nanoparticles might be suitable for bio-imaging tags in dark-field microscopy techniques [30]. For comparison, we display the absorption of whole

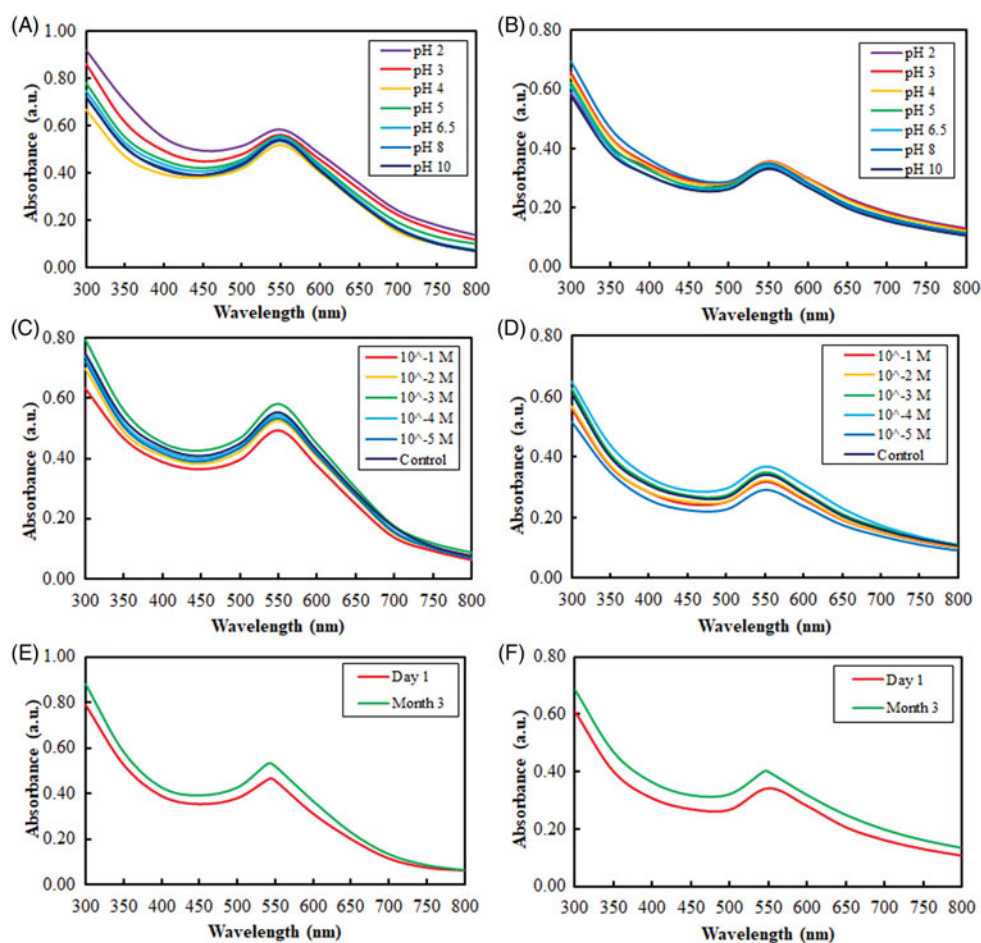


**Figure 5.** UV-vis absorbance spectra of the obtained nanoparticles depicting their high stability in various conditions due to protein capping. Stability of DCY51<sup>T</sup>-AuNps and DCY51<sup>T</sup>-AuCKNps against varied pH conditions (A, B) and electrolytic concentrations (C, D) and three-month storage (E, F), respectively.

cells and a sample where nanoparticles were continuously reduced within or on the surface of bacterial cells [33]. As expected, whole cells of *L. kimchicus* DCY51<sup>T</sup> did not contribute to the peaks observed in DCY51<sup>T</sup>-AuNps and DCY51<sup>T</sup>-AuCKNps. In addition, the lack of change in the SPR peak and band, as measured by UV-vis spectrometry, after incubation at different pH values and ion strengths indicated the good colloidal stability of the nanoparticles in all of the conditions (Figure 5(A-D)) [30]. Furthermore, DCY51<sup>T</sup>-AuNps and DCY51<sup>T</sup>-AuCKNps were stable for 3 months at room temperature with no significant changes in absorbance values or aggregation states in the suspensions (Figure 5(E,F)). These results confirmed the colloidal stability of DCY51<sup>T</sup>-AuNps and DCY51<sup>T</sup>-AuCKNps by *L. kimchicus* DCY51<sup>T</sup> in all of the above experimental conditions. To boot, the colloidal stability of DCY51<sup>T</sup>-AuNps and DCY51<sup>T</sup>-AuCKNps in aqueous medium was substantiated by the relatively high  $\zeta$ -potential; high magnitude of  $\zeta$ -potential indicates that the nanoparticles will resist aggregation resulted by electrostatic repulsion between nanoscale particles [42].

The crystalline nature of the biologically synthesized nanoparticles was evaluated by XRD analysis. Figure 4(B) demonstrates the intensive diffraction patterns of biosynthesized DCY51<sup>T</sup>-AuCKNps. The four characteristic peaks of gold were indexed to the (111), (200), (220) and (311) lattice planes of Bragg's reflection. The most intense peak at (111) proves that

DCY51<sup>T</sup>-AuCKNps were composed of (111) lattice plane. The selected area electron diffraction (SAED) pattern likewise confirmed the polycrystalline orientation of the nanoparticles as shown in the multi-faceted rings in Figure 2(D). The average metallic diameter of DCY51<sup>T</sup>-AuCKNps was estimated by taking the full width at half maximum (FWHM) of the most intense peak (111); the resulting nanoparticles maintained an average crystallite diameter of  $\sim 6.04$  nm. Photoluminescence spectroscopy was performed. The intensity of DCY51<sup>T</sup>-AuCKNps at 425 nm is shown in Figure 4(C).

### FTIR profile analysis of DCY51<sup>T</sup>-AuCKNps

In our previous study by Markus et al., we proposed that EPS and/or enzymes secreted on the bacterial membrane and amino acid residues inside the cells were responsible for playing both the roles of reducing agent and stabilizers to DCY51<sup>T</sup>-AuNps via electrostatic interactions between the oxidized carboxylate (COO<sup>-</sup>) groups of the enzymes and the surface of nanoparticles (Au-COO<sup>-</sup>) [20]. Additionally, several absorption peaks of *L. kimchicus* DCY51<sup>T</sup> and DCY51<sup>T</sup>-AuNps were also present in the FTIR spectrum of DCY51<sup>T</sup>-AuCKNps (tabulated in Figure 6), namely the strong characteristic peak of carbonyl (C=O) stretching of amide at 1650 cm<sup>-1</sup> and the medium characteristic peak of amine (N-H) bending at

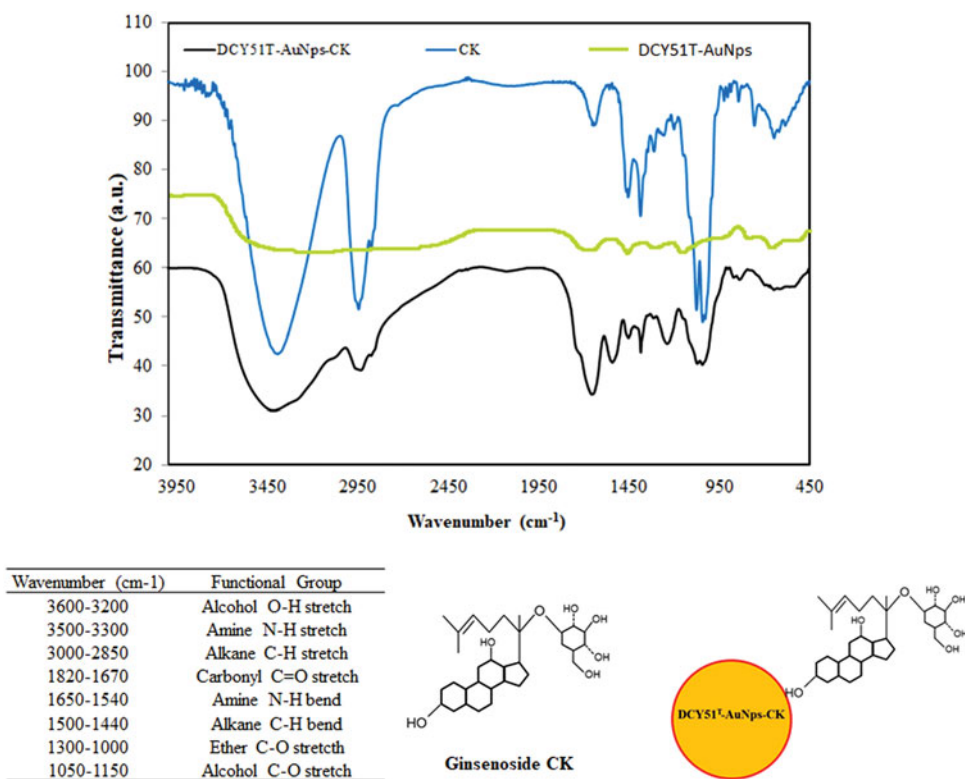


**Figure 6.** FTIR spectra of DCY51<sup>T</sup>-AuCKNps and proposed ginsenoside CK complexation onto the surface of DCY51<sup>T</sup>-AuNps. FT-IR spectra of DCY51<sup>T</sup>-AuCKNps revealed the presence of C–H bends (alkane groups) and C–O stretch (ethers) of ginsenoside CK.

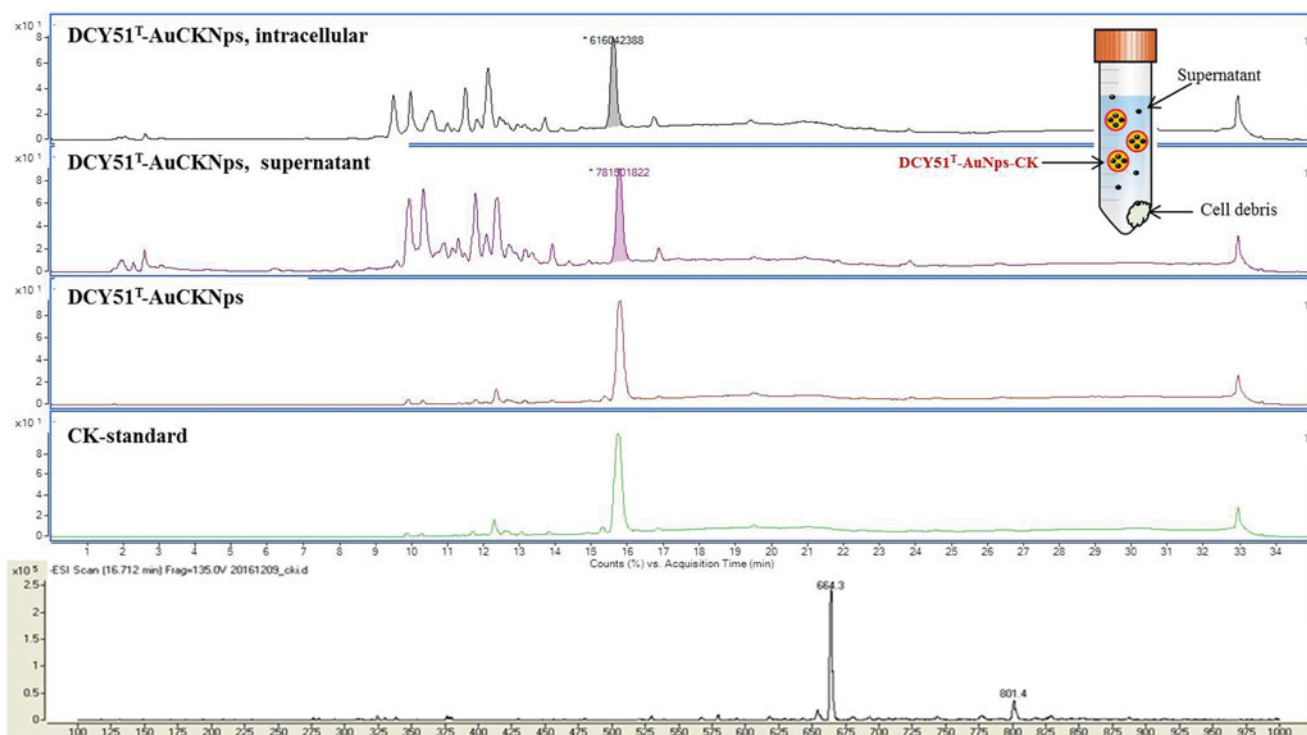


**Figure 7.** LC–MS spectra of ginsenoside CK released from DCY51<sup>T</sup>-AuCKNps after 24 h of sonication in DMSO–MeOH mixture (1:4, v/v). Inset distinguishes the ginsenoside CK released from the intracellular content of cell debris, supernatant, and purified DCY51<sup>T</sup>-AuCKNps.

1540 cm<sup>-1</sup> contributed by the proteins and amino acid residues of *L. kimchicus* DCY51<sup>T</sup> [43–45].

The complexation of ginsenoside CK on the surface of DCY51<sup>T</sup>-AuCKNps was confirmed by the peaks corresponding to alkane (C–H) bending at 1500–1440 cm<sup>-1</sup> and aliphatic

ether (C–O) stretching at 1300–1000 cm<sup>-1</sup> of ginsenoside CK [46]. These peaks were suspected to be the result of the non-covalent attractive forces (i.e. electrostatic interactions, hydrogen bonds, hydrophobic forces and van der Waals forces) between ginsenoside CK and DCY51<sup>T</sup>-AuNps: following

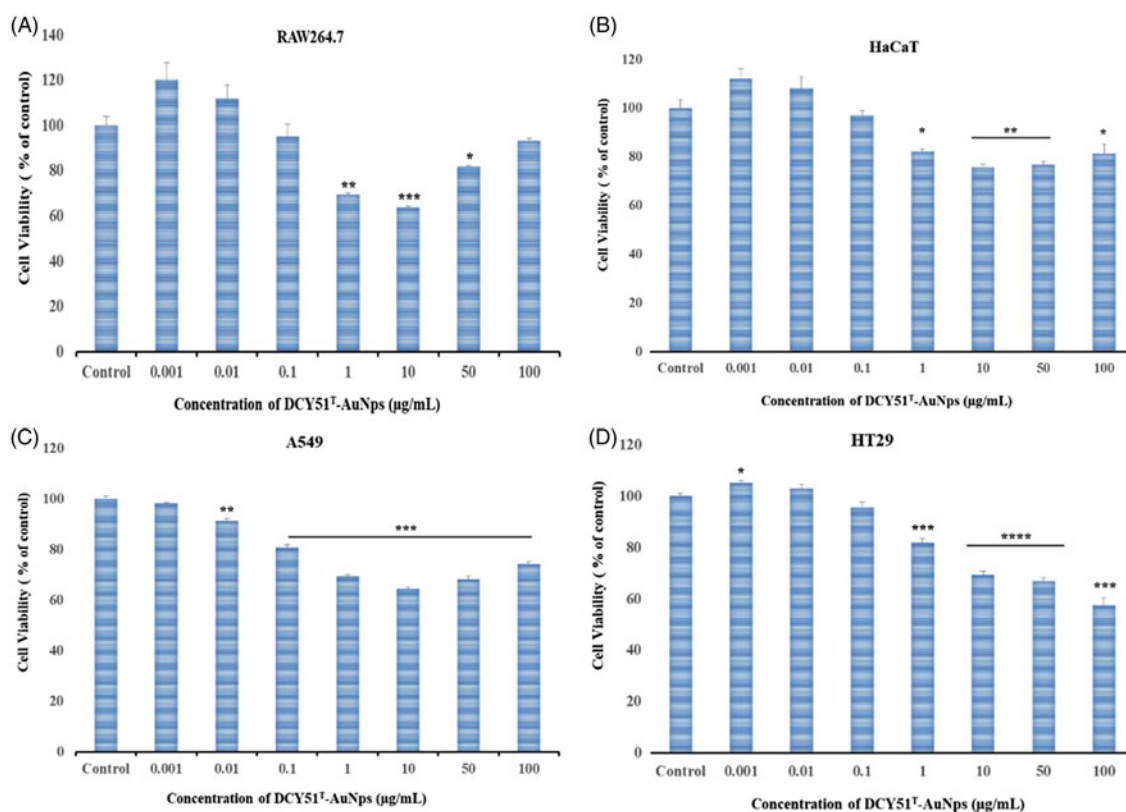


**Figure 8.** Cytotoxicity of DCY51<sup>T</sup>-AuNPs after 48 h of incubation. (A) Macrophage cell line RAW264.7. (B) Keratinocyte cell line HaCaT. (C) Lung cancer cell line A549. (D) Colon cancer cell line HT29. Results are presented as means  $\pm$  SDs.

nucleation and stabilization by surface-bound enzymes, ginsenoside CK might form stable interactions with the amino acid residues on the surface of DCY51<sup>T</sup>-AuNPs. In addition, the hydroxyl groups of ginsenoside CK might act as additional reducing species for the reduction of Au<sup>3+</sup> ions into Au<sup>0</sup> and oxidize into carboxylates as shown in the inset of Figure 6.

#### Drug loading efficiency via LC-MS and Au ion content

Quantification of the concentration of ginsenoside CK in the drug-loaded DCY51<sup>T</sup>-AuCKNPs is a critical parameter to evaluate the properties of the nanoformulations (Figure 7). DCY51<sup>T</sup>-AuCKNPs were exposed to a DMSO-MeOH mixture (1:4, v/v) and sonication at room temperature overnight to allow complete release of ginsenoside CK and evaluation of the drug loading efficiency. The majority of the released drug was expected to be dissolved in the MeOH fraction because of the high solubility in MeOH [47]. Following sonication, approximately 110.30 µg of ginsenoside CK per one mg of DCY51<sup>T</sup>-AuCKNPs was released in the medium. A calibration curve was prepared of a CK standard with known concentrations in the range of 10–100 µg/mL (regression equation:  $y = 1,203,623.2951x + 8,433,298.2623$ ;  $R^2 = 99.86\%$ ). Thus, the drug loading efficiency was determined to be  $\sim 11.03\%$ . The released CK from DCY51<sup>T</sup>-AuCKNPs was subjected to mass spectroscopy to determine its molecular weight. The molecular weight of the ginsenoside obtained from DCY51<sup>T</sup>-AuCKNPs was determined to be 618.3 which is similar to the molecular weight of CK (622.88) (mass spectrum of CK,

$m/z = 664.3 = [MW + \text{formic acid}]$ , MW 618.3). The Au (MW 197) content of DCY51<sup>T</sup>-AuCKNPs was 104 µg/g DCY51<sup>T</sup>-AuCKNPs, as measured by ICP/OES [26].

#### In vitro cell cytotoxicity of DCY51<sup>T</sup>-AuCKNPs by MTT assay

The results of MTT assay for DCY51<sup>T</sup>-AuNPs are shown in Figure 8. We observed a different *in vitro* cytotoxicity profiles in RAW264.7 and HT29 than those previously observed in our prior study [20]. We conjectured that washing the biosynthesized gold nanoparticles with 80% MeOH, which was conducted in our prior study, might promote the dynamic unbinding of bioactive compounds from the nanoparticles surface and thus reducing their biological activity. Additionally, DCY51<sup>T</sup>-AuNPs were air-dried and re-dispersed in water before analysis; air-drying might cause the nanoparticles to irreversibly aggregate which influenced their toxicities. In view of these factors, DCY51<sup>T</sup>-AuNPs and DCY51<sup>T</sup>-AuCKNPs were washed with dH<sub>2</sub>O and stored as aqueous suspensions at 4 °C to prevent unwanted decomplexation and aggregation prior to analyses.

Upon close observation, the viability of the cells in RAW264.7 and HaCaT cell lines bounced back as the viability of the cells decreased significantly at 1 µg/mL ( $69.38 \pm 1.80\%$  and  $82.32 \pm 1.47\%$ , respectively) and started to increase to  $93.33 \pm 1.94\%$  and  $81.42 \pm 7.51\%$ , respectively, at 100 µg/mL (Figure 8(A,B)). Moreover, cell viability of A549 cells was significantly inhibited to  $69.38 \pm 1.05\%$  at 1 µg/mL,  $64.40 \pm 1.27\%$  at 10 µg/mL,  $68.18 \pm 2.44\%$  at 50 µg/mL and

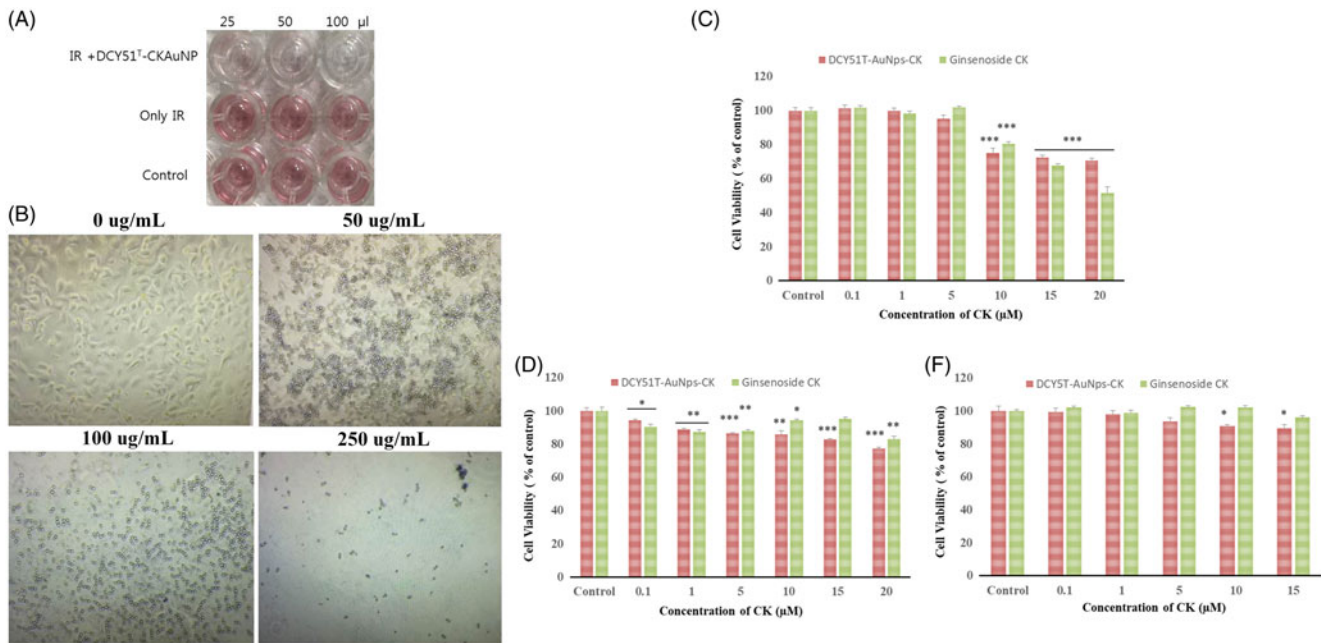


**Figure 9.** Antiproliferative activity (MTT assay) (A) of DCY51<sup>T</sup>-AuCNPs on the cancer cell lines with and without treatment (B). Cytotoxicity of DCY51<sup>T</sup>-AuCNPs and ginsenoside CK after 48 h of incubation. (A) Macrophage cell line RAW264.7. (B) Lung cancer cell line A549. (C) Colon cancer cell line HT29. Results are presented as means  $\pm$  SDs.

finally to  $74.24 \pm 2.32\%$  at  $100 \mu\text{g/mL}$  (Figure 8(C)). On the other hand, HT29 cells showed a dose-dependent cell inhibition as the cell viability was inhibited to  $81.90 \pm 2.96\%$  at  $1 \mu\text{g/mL}$  and finally to  $57.67 \pm 5.30\%$  at  $100 \mu\text{g/mL}$  (Figure 8(D)).

The cytotoxicity of DCY51<sup>T</sup>-AuCNPs and standard ginsenoside CK was evaluated in RAW264.7 and cancer (A549 and HT29) cell lines via MTT assay. The results are shown in Figure 8. Sufficient concentrations of DCY51<sup>T</sup>-AuCNPs were used such that the concentration of CK in the free drug was equivalent to that in the drug-loaded nanoparticles. Based on MTT results, DCY51<sup>T</sup>-AuCNPs were found to exert less cytotoxicity compared to free CK in RAW264.7 (Figure 8(A)). At  $20 \mu\text{M}$  of equivalent CK content (or  $113 \mu\text{g/mL}$  of DCY51<sup>T</sup>-AuCNPs), DCY51<sup>T</sup>-AuCNPs inhibited the cell viability to  $70.74 \pm 2.49\%$  while free drug inhibited the cell viability to  $51.60 \pm 7.37\%$ , suggesting that the systemic cytotoxicity of CK in RAW264.7 cells was reduced in DCY51<sup>T</sup>-AuCNPs (Figure 8(A)). However, DCY51<sup>T</sup>-AuCNPs demonstrated greater cell inhibition in RAW264.7 cells starting at  $10 \mu\text{M}$  ( $75.24 \pm 5.41\%$ ) of equivalent ginsenoside CK content compared to A549 ( $85.87 \pm 4.32\%$ ) and HT29 ( $90.91 \pm 1.70\%$ ) cells. Moreover, loading of ginsenoside CK seemed to reduce the overall inhibition activity of DCY51<sup>T</sup>-AuNps in HT29 cells. DCY51<sup>T</sup>-AuCNPs exhibited slightly higher cytotoxicity in A549 and HT29 cells compared to free drug starting at  $5 \mu\text{M}$  of equivalent CK content, which did not exert significant cytotoxicity in RAW264.7 cells (Figure 8(B,C)). The antiproliferative activity of DCY51<sup>T</sup>-AuCNPs towards the stomach cancer cell line (AGS) was also evaluated using an MTT assay after treatment with an IR beam (Figure 9(A)). Purple formazan crystals formed in control wells and IR-irradiated wells (negative control wells), whereas the DCY51<sup>T</sup>-AuCNPs-treated wells showed little purple colour ( $50 \mu\text{L}$ ), slight

discolouration ( $100 \mu\text{L}$ ) and finally colourless solution ( $250 \mu\text{L}$ ) after IR treatment suggesting that cell viability was inhibited in cancer cells in a dose-dependent manner (Figure 9(B)). Additionally, disintegrated cancer cells after treatment of DCY51<sup>T</sup>-AuCNPs and IR beam in a dose-dependent manner was also observed (Figure 9(B)).

For the following *in vitro* PPT experiment, the use of DCY51<sup>T</sup>-AuCNPs at  $1$  and  $5 \mu\text{g/mL}$  (equivalent to  $0.18$  and  $0.89 \mu\text{M}$  of CK) was selected since within this concentration range DCY51<sup>T</sup>-AuCNPs did not exert strong cytotoxicity towards RAW264.7 cells as observed in Figure 9(C–E).

### **In vitro photothermal therapy and apoptosis detection**

As the result of the EPR effect, DCY51<sup>T</sup>-AuCNPs may accumulate in tumour tissues due to leaky vasculatures. Once accumulated, cationic DCY51<sup>T</sup>-AuCNPs may be taken up inside the cells by receptor-independent endocytosis through interaction with the cell membrane [48]. Ginsenoside CK may then be released by lysosomal degrading enzymes, while DCY51<sup>T</sup>-AuNps are expected to retain their stability in a low acidic environment. The detection of intracellular DCY51<sup>T</sup>-AuCNPs in stomach cancer cells (AGS) presumably uptake via receptor-independent endocytosis can be observed in the images in Figure 10. Differential interference contrast and dark field images showed clearly intracellular DCY51<sup>T</sup>-AuCNPs particles from treated AGS cell lines (Figure 10(C)), whereas untreated AGS cell lines never showed any traces of intracellular DCY51<sup>T</sup>-AuCNPs. In addition, DCY51<sup>T</sup>-AuCNPs can be irradiated at mild wavelength to rapidly induce cell lysis due to the elevated temperature induced by light-to-heat conversion (hyperthermia). Localized heat treatment utilizing temperatures over  $40^\circ\text{C}$  has been reported to damage tumour cells irreversibly by inducing protein degradation and

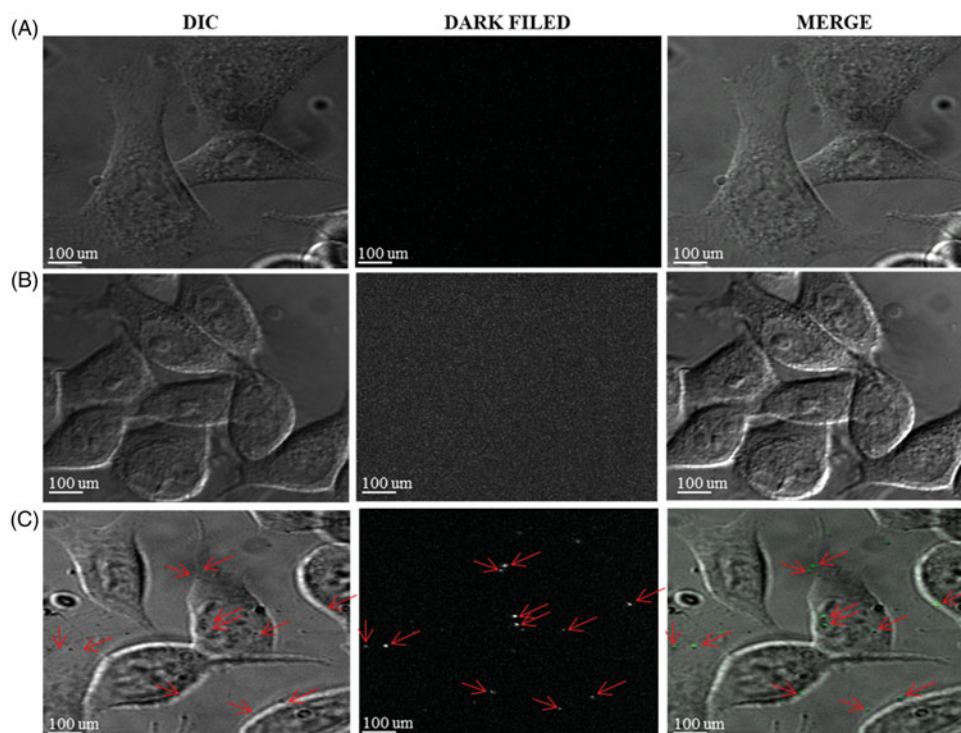


**Figure 10.** Detection of intercellular DCY51<sup>T</sup>-AuCKNps in the stomach cancer cell lines (AGS). (A) Control sample, (B) 800 nm laser treatment for 10 min. (C) DCY51<sup>T</sup>-AuCKNps + laser at 800 nm for 10 min.

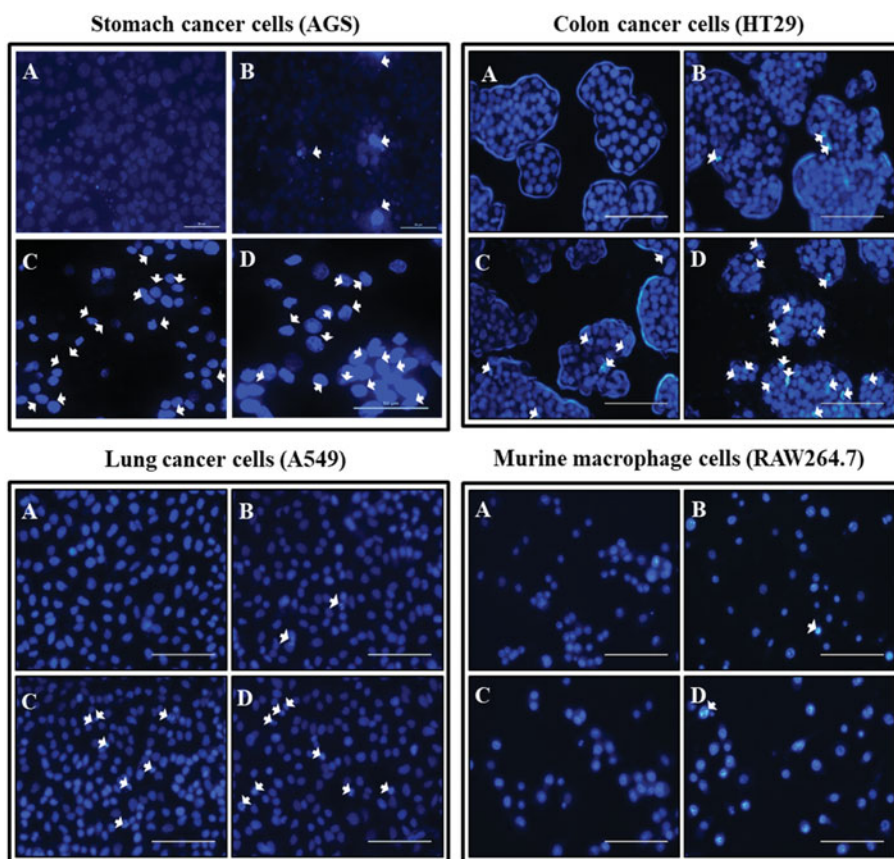


**Figure 11.** Fluorescent images of cells stained with Hoechst stain after an incubation time of Ankrum h. (A) Blank. (B) DCY51<sup>T</sup>-AuNps; 5  $\mu\text{g}/\text{mL}$ . (C) DCY51<sup>T</sup>-AuCKNps; 1  $\mu\text{g}/\text{mL}$ . (D) DCY51<sup>T</sup>-AuCKNps; 5  $\mu\text{g}/\text{mL}$ . Apoptotic cells are indicated with white arrows. The scale bar equals 10  $\mu\text{m}$ . There were more apoptotic cells in the DCY51<sup>T</sup>-AuCKNps groups than in blank or in the negative control (DCY51<sup>T</sup>-AuNps). The co-treatment groups of hyperthermia and chemotherapy exhibited the greatest number of apoptosis in cancer cells.

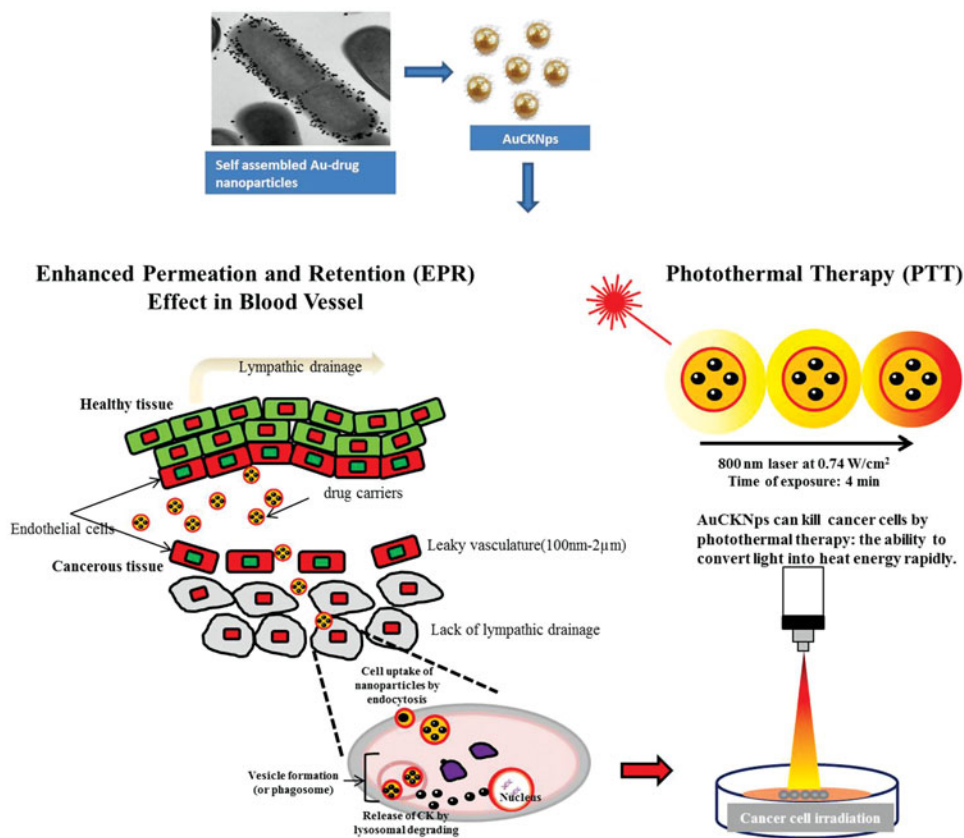


**Figure 12.** The proposed mechanism of cell internalization of DCY51<sup>T</sup>-AuCKNps by the EPR effect and *in vitro* photothermal therapy. DCY51<sup>T</sup>-AuCKNps reaches the cell membrane by exploiting the properties of the EPR effect. Following association with the cell by endocytosis, DCY51<sup>T</sup>-AuCKNps may aggregate on the anionic surface of cancer cells due to the cationic surface charge of the nanoparticles. In conjunction, DCY51<sup>T</sup>-AuCKNps can be irradiated to rapidly induce cell lysis.

DNA repair deficiency [49]. To investigate the photothermal effects of DCY51<sup>T</sup>-AuCKNps, a 635 nm laser at a heat flux density of 0.74 W/cm<sup>2</sup> was used to irradiate RAW264.7 cell and cancer cell (A549 and HT29) lines. AGS cells were irradiated with 800 nm laser. To specifically analyse the photothermal effects, Hoechst staining was applied. As shown in Figure 11, the fluorescent images showed that the blank group, which was irradiated with the laser treatment alone, exhibited no apoptosis. As predicted, incubation with DCY51<sup>T</sup>-AuNps (negative control) induced a slight apoptosis in the RAW264.7 and cancer cells (A549 and HT29) because they caused cell inhibition within this concentration range (5 µg/mL), as demonstrated by MTT results.

However, the number of apoptotic cells in the DCY51<sup>T</sup>-AuCKNps groups was significantly higher than those in the DCY51<sup>T</sup>-AuNps groups at the same concentration (5 µg/mL). Moreover, cells incubated with DCY51<sup>T</sup>-AuCKNps (both 1 and 5 µg/mL) were shown to demonstrate higher apoptosis in stomach, lung and colon adenocarcinoma cells than RAW264.7 cells. Increasing the concentration of DCY51<sup>T</sup>-AuCKNps from 1 to 5 µg/mL also resulted in higher apoptotic cells in cancer cell lines. We have also established increasing cell apoptotic mediated cell death in stomach cancer cell line (AGS) through a dose-dependent manner by staining the AGS cell lines with propidium iodide (Supplementary Figure S1). The cells treated with DCY51<sup>T</sup>-AuCKNps and laser treatment caused cell damages which led to dead cells. Staining

the dead cells with propidium iodide resulted in the appearance of red fluorescence.

This finding suggests that DCY51<sup>T</sup>-AuCKNps have the potential to increase apoptosis in cancer cells in conjunction with photo-induced hyperthermia more than chemotherapy alone, possibly due to the increased sensitivity of tumour cells to ginsenoside or light-triggered drug release into cancer cells [6, 7, 49]. The proposed mechanism of cell internalization of DCY51<sup>T</sup>-AuCKNps by the EPR effect and *in vitro* PPT is demonstrated in Figure 12.

Several studies have reported that when conjugated with drugs, gold nanoparticles can function as drug carriers to enhance the release and uptake of drugs by tumour tissues undergoing hyperthermia stimulation [50]. Despite the lower toxicity of gold nanoparticles compared with other metallic nanoparticles, their lack of clearance from the body still remains an issue [50]. Specific targeting of cancer cells and minimizing the risk of *in vivo* toxicity are the main challenges of this study and must be thoroughly addressed prior to *in vivo* experiments [51].

## Conclusions

In summary, this study highlights the development of ginsenoside CK-gold nanocarriers (DCY51<sup>T</sup>-AuCKNps) via an intracellular membrane-bound mechanism by lactic acid-producing *Lactobacillus kimchicus* DCY51<sup>T</sup>. Ginsenoside CK

was effectively loaded onto the surface of gold nanoparticles by non-covalent conjugation such as, electrostatic forces, hydrogen bonding, hydrophobic forces and van der Waals interactions. Upon further investigation by HR-TEM, the particles were formed in the bacterial capsule and cell wall than on the cytoplasmic membrane, possibly due to reduction of the metal ions by enzymes and EPSs present in the cell wall and slime layer. The drug loading efficiency was determined to be ~11.03%. The FTIR spectra of DCY51<sup>T</sup>-AuCKNps demonstrated the presence of alkane (C–H) bending and ether (C–O) stretching of ginsenoside CK, further confirming the direct complexation of ginsenoside to the surface of nanoparticles. The *in vitro* stability of DCY51<sup>T</sup>-AuNps and DCY51<sup>T</sup>-AuCKNps demonstrated their resistance to aggregation and dissociation caused by pH variation or a high ionic strength environment. Although DCY51<sup>T</sup>-AuCKNps demonstrated greater cell inhibition in RAW264.7 cells at 10–20 μM of equivalent ginsenoside CK concentration compared to A549 and HT29 cells at the same concentrations, preferential cytotoxicity of DCY51<sup>T</sup>-AuCKNps against A549 cells and HT29 compared to free ginsenoside CK was demonstrated by MTT assays. Increased apoptosis of DCY51<sup>T</sup>-AuCKNps in cancer cells compared to cell apoptosis count in RAW264.7 cells and DCY51<sup>T</sup>-AuNps-treated cells at sublethal concentrations was confirmed by Hoechst staining with excitations by laser. These results suggest that DCY51<sup>T</sup>-AuCKNps are promising drug delivery platforms for cancer therapy as novel photo-thermal and chemotherapeutic agents.

## Disclosure statement

No potential conflict of interest was reported by the author(s).

## Funding

This work was supported by Nano Conversion Foundation funded by the Ministry of Science and ICT (MSIT, Korea) and the Ministry of Trade, Industry and Energy (MOTIE, Korea) (Project No. R201800510) and the support of "Cooperative Research Program for Agriculture Science and Technology Development (Project No. PJ0128132017)" Rural Development Administration, Republic of Korea.

## References

- [1] Kim DH. Gut microbiota-mediated pharmacokinetics of ginseng saponins. *J Ginseng Res.* 2018;42(3):255–263.
- [2] Kim DH. Metabolism of ginsenosides to bioactive compounds by intestinal microflora and its industrial application. *J Ginseng Res.* 2009;33:165–176.
- [3] Mathiyalagan R, Subramaniam S, Kim YJ, et al. Ginsenoside compound K-bearing glycol chitosan conjugates: synthesis, physico-chemical characterization, and *in vitro* biological studies. *Carbohydr Polym.* 2014;112:359–366.
- [4] Voruganti S, Qin JJ, Sarkar S, et al. Oral nano-delivery of anti-cancer ginsenoside 25-OCH<sub>3</sub>-PPD, a natural inhibitor of the MDM2 oncogene. Nanoparticle preparation, characterization, *in vitro* anti-prostate cancer activity and mechanism of action. *Oncotarget.* 2015;6:21379–21394.
- [5] Yang ZS, Gao J, Wang T, et al. Enhancement of oral bioavailability of 20(S)-ginsenoside Rh<sub>2</sub> through improved understanding of its absorption and efflux mechanisms. *Drug Metab Dispos.* 2011;39:1866–1872.
- [6] Kautzka Z, Clement S, Goldys EM, et al. Light-triggered liposomal cargo delivery platform incorporating photosensitizers and gold nanoparticles for enhanced singlet oxygen generation and increased cytotoxicity. *IJN.* 2017;12:969–977.
- [7] Yeo ELL, Joshua U, Cheah J, et al. Exploiting the protein corona around gold nanorods for low-dose combined photothermal and photodynamic therapy. *J Mater Chem B.* 2017;5:254–268.
- [8] Leonard K, Ahmmad B, Okamura H, et al. In situ green synthesis of biocompatible ginseng capped gold nanoparticles with remarkable stability. *Colloids Surf B Biointerfaces.* 2011;82:391–396.
- [9] Shanmugam V, Selvakumar S, Yeh CS. Near-infrared light-responsive nanomaterials in cancer therapeutics. *Chem Soc Rev.* 2014;43:6254–6287.
- [10] Alkilany AM, Thompson LB, Boulos SP, et al. Gold nanorods: their potential for photothermal therapeutics and drug delivery, tempered by the complexity of their biological interactions. *Adv Drug Deliv Rev.* 2012;64:190–199.
- [11] Zhang Z, Wang J, Chen C. Near-infrared light-mediated nanoplat-forms for cancer thermo-chemotherapy and optical imaging. *Adv Mater.* 2013;25:3869–3880.
- [12] Hu SH, Fang RH, Chen YW, et al. Photoresponsive protein-graphene hybrid capsules with dual targeted heat triggered drug delivery approach for enhanced tumor therapy. *Adv Funct Mater.* 2014;24:4144–4155.
- [13] Ma Y, Liang X, Tong S, et al. Gold nanoshell nanomicelles for potential magnetic resonance imaging, light-triggered drug release and photothermal therapy. *Adv Funct Mater.* 2013;23:815–822.
- [14] Chen Q, Liang C, Wang C, et al. An imagable and photothermal "Abraxane-like" nanodrug for combination cancer therapy to treat subcutaneous and metastatic breast tumors. *Adv Mater.* 2015;27:903–910.
- [15] Zhang Z, Wang J, Nie X, et al. Near infrared laser-induced targeted cancer therapy using thermoresponsive polymer encapsulated gold nanorods. *J Am Chem Soc.* 2014;136:7317–7326.
- [16] Okuno T, Kato S, Hatakeyama Y, et al. Photothermal therapy of tumors in lymph nodes using gold nanorods and near-infrared laser light. *J Control Release.* 2013;172:879–884.
- [17] Iravani S. Bacteria in nanoparticle synthesis: current status and future prospects. *Int Sch Res Notices.* 2014;2014:359316.
- [18] Nair B, Pradeep T. Coalescence of nanoclusters and formation of submicron crystallites assisted by *Lactobacillus* strains. *Cryst Growth Des.* 2002;2:293–298.
- [19] Liang ZQ, Srinivasan S, Kim YJ, et al. *Lactobacillus kimchicus* sp. nov., a β-glucosidase-producing bacterium isolated from kimchi. *Int J Syst Evol Microbiol.* 2011;61:894–897.
- [20] Markus J, Mathiyalagan R, Kim YJ, et al. Intracellular synthesis of gold nanoparticles with antioxidant activity by probiotic *Lactobacillus kimchicus* DCY51<sup>T</sup> isolated from Korean Kimchi. *Enzyme Microb Technol.* 2016;95:85–93.
- [21] Singh P, Kim YJ, Wang C, et al. Microbial synthesis of flower shaped gold nanoparticles. *Artif Cells Nanomed Biotechnol.* 2015;44:1–1474.
- [22] Haiss W, Thanh NT, Aveyard J, et al. Determination of size and concentration of gold nanoparticles from UV-vis spectra. *Anal Chem.* 2007;79:4215–4221.
- [23] Hu Y, Liu W, Wu F. Novel multi-responsive polymer magnetic microgels with folate or methyltetrahydrofolate ligand as anti-cancer drug carriers. *RSC Adv.* 2017;7:10333–10344.
- [24] Madhusudhan A, Reddy GB, Venkatesham M, et al. Efficient pH dependent drug delivery to target cancer cells by gold nanoparticles capped with carboxymethyl chitosan. *Int J Mol Sci.* 2014;15:8216–8234.
- [25] Tannock IF, Rotin D. Acid pH in tumors and its potential for therapeutic exploitation. *Cancer Res.* 1989;49:4373–4384.
- [26] Khan N, In S, Jeong IS, et al. Analysis of minor and trace elements in milk and yogurts by inductively coupled plasma-mass spectrometry (ICP-MS). *Food Chem.* 2014;147:220–224.
- [27] Aceituno VC, Ahn S, Simu SY, et al. Silver nanoparticles from *Dendropanax moribifera* Lévaille inhibit cell migration, induce

- apoptosis, and increase generation of reactive oxygen species in A549 lung cancer cells. *In Vitro Cell Dev Biol Anim.* 2016;52:1012–1019.
- [28] Ahn S, Siddiqi MH, Aceituno VC, et al. Ginsenoside Rg5:Rk1 attenuates TNF- $\alpha$ /IFN- $\gamma$ -induced production of thymus- and activation-regulated chemokine (TARC/CCL17) and LPS-induced NO production via downregulation of NF- $\kappa$ B/p38 MAPK/STAT1 signaling in human keratinocytes and macrophages. *In Vitro Cell Dev Biol Anim.* 2016;52:287–295.
- [29] Wang D, Markus J, Kim YJ, et al. Coalescence of functional gold and monodisperse silver nanoparticles mediated by black *Panax ginseng* Meyer root extract. *IJN.* 2016;11:6621–6634.
- [30] Markus J, Kim YJ, Wang C, et al. Biosynthesis, characterization, and bioactivities evaluation of silver and gold nanoparticles mediated by the roots of Chinese herbal *Angelica pubescens Maxim.* *Nanoscale Res Lett.* 2017;12:46.
- [31] Lee SA, Kang SH. Fluorescent-free detection on nanobiochips based on wavelength-dependent single plasmonic nanoparticles by differential interference contrast microscopy. *Biosens Bioelectron.* 2014;60:45–51.
- [32] Shedbalkar U, Singh R, Wadhvani S, et al. Microbial synthesis of gold nanoparticles: current status and future prospects. *Adv Colloid Interface Sci.* 2014;209:40–48.
- [33] Mittal AK, Kaler A, Mulay AV, et al. Synthesis of gold nanoparticles using whole cells of *Geotrichum candidum*. *J Nanopart.* 2013; 2013:1.
- [34] Jazayeri MH, Amani H, Pourfatollah AA, et al. Various methods of gold nanoparticles (GNPs) conjugation to antibodies. *Sens Biosens Res.* 2016;9:17–22.
- [35] Singh P, Singh H, Aceituno VC, et al. Bovine serum albumin as a nanocarrier for the efficient delivery of ginsenoside compound K: preparation, physicochemical characterizations and *in vitro* biological studies. *RSC Adv.* 2017;7:15397–15407.
- [36] Wang C, Mathiyalagan R, Kim YJ, et al. Rapid green synthesis of silver and gold nanoparticles using *Dendropanax morbifera* leaf extract and their anticancer activities. *IJN.* 2016;11:3691–3701.
- [37] Upadhyaya L, Singh J, Agarwal V, et al. Efficient water soluble nanostructured ZnO grafted O-carboxymethyl chitosan/curcumin-nanocomposite for cancer therapy. *Process Biochem.* 2015;50: 678–688.
- [38] Kishen A. Current and potential clinical applications. In: *Nanotechnology in endodontics.* Switzerland: Springer International Publishing; 2015.
- [39] Poon RT, Borys N. Lyso-thermosensitive liposomal doxorubicin: a novel approach to enhance efficacy of thermal ablation of liver cancer. *Expert Opin Pharmacother.* 2009;10:333–343.
- [40] Ramamurthy C, Padma M, Mareeswaran R, et al. The extra cellular synthesis of gold and silver nanoparticles and their free radical scavenging and antibacterial properties. *Colloids Surf B Biointerfaces.* 2013;102:808–815.
- [41] Rahman S. Size and concentration analysis of gold nanoparticles with ultraviolet-visible spectroscopy. *Undergrad J Math Model.* 2016;2(1): Article 2.
- [42] Hoskins C, Min Y, Gueorguieva M, et al. Hybrid gold-iron oxide nanoparticles as a multifunctional platform for biomedical application. *J Nanobiotechnol.* 2012;10:27.
- [43] Bhattacharjee S. DLS and zeta potential – what they are and what they are not? *J Control Release.* 2016;235:337–351.
- [44] Debnath R, Purkayastha DD, Hazra S, et al. Biogenic synthesis of antioxidant, shape selective gold nanomaterials mediated by high altitude lichens. *Mater Lett.* 2016;169:58–61.
- [45] Elbeshehy EK, Elazzazy AM, Aggelis G. Silver nanoparticles synthesis mediated by new isolates of *Bacillus* spp., nanoparticle characterization and their activity against Bean Yellow Mosaic Virus and human pathogens. *Front Microbiol.* 2015;6:453.
- [46] Kumar CS, Raja M, Sundar DS, et al. Hyaluronic acid co-functionalized gold nanoparticle complex for the targeted delivery of metformin in the treatment of liver cancer (HepG2 cells). *Carbohydr Polym.* 2015;128:63–74.
- [47] Li P, Zhou X, Qu D, et al. Preliminary study on fabrication, characterization and synergistic anti-lung cancer effects of self-assembled micelles of covalently conjugated celastrol-polyethylene glycol-ginsenoside Rh2. *Drug Deliv.* 2017;24:834–845.
- [48] Ankrum JA, Miranda OR, Ng KS, et al. Engineering cells with intracellular agent-loaded microparticles to control cell phenotype. *Nat Protoc.* 2014;9:233–245.
- [49] Fröhlich E. The role of surface charge in cellular uptake and cytotoxicity of medical nanoparticles. *Int J Nanomedicine.* 2012;7: 5577–5591.
- [50] Zhang AW, Guo WH, Qi YF, et al. Synergistic effects of gold nanocages in hyperthermia and radiotherapy treatment. *Nanoscale Res Lett.* 2016;11:279.
- [51] Lee J, Chatterjee DK, Lee MH, et al. Gold nanoparticles in breast cancer treatment: promise and potential pitfalls. *Cancer Lett.* 2014;347:46–53.